Towards a Harmonized Operational Earthquake Forecasting Model for Europe

Marta Han[1], Leila Mizrahi[1], and Stefan Wiemer[1]

[1]Swiss Seismological Service (SED), ETH Zurich, Switzerland

Correspondence: Marta Han (marta.han@sed.ethz.ch)

Abstract. We develop a harmonized earthquake forecasting model for Europe based on the Epidemic-type Aftershock Sequence (ETAS) model to describe the spatio-temporal evolution of aftershock sequences. We propose a method modification that integrates information from the European Seismic Hazard Model (ESHM20) about the spatial variation of background seismicity during ETAS parameter inversion based on the expectation–maximization (EM) algorithm. Other modifications to the basic ETAS model are explored, namely fixing the productivity term to a higher value to balance the more productive triggering by high-magnitude events with their much rarer occurrence, and replacing the b-value estimate with one relying on the b-positive method to observe the possible effect of short-term incompleteness on model parameters. Retrospective and pseudo-prospective tests demonstrate that ETAS-based models outperform the time-independent benchmark model as well as an ETAS model calibrated on global data. The background-informed ETAS variant achieves the highest score in the pseudo-prospective experiment, but the performance difference to the second-best model is not significant. Our findings highlight promising areas for future exploration, such as avoiding the simplification of using a single b-value for the entire region or reevaluating the completeness of the used seismic catalogs.

1   Introduction

After the occurrence of a large-magnitude earthquake, the expected behavior of its aftershocks, and in particular the possibility of another large event, are of interest both to the general public and governmental and private organisations, such as civil protection, first responders, insurance companies, etc. Operational Earthquake Forecasting (OEF; Jordan et al., 2011) was introduced as a term for *"gathering and disseminating authoritative information about the time dependence of seismic hazards to help communities prepare for potentially destructive earthquakes"*. It is an evolving effort that has seen significant progress in recent years. Several countries, including New Zealand (Christophersen et al., 2017), the United States (Field et al., 2017; Jordan et al., 2011, 2014; van der Elst et al., 2022), and Italy (Marzocchi and Lombardi, 2009; Marzocchi et al., 2014) currently have systems in place that produce authoritative earthquake forecasts. Each of these systems uses different underlying models to produce the forecasts, communicates the forecasts differently and to different user groups, and the forecasting systems are continuously being modified and improved. There is not a unique agreed-upon best way to provide OEF, as has been shown recently in an elicitation of expert views on this topic (Mizrahi et al., 2023a).

25 However, what is clear is that to issue earthquake forecasts operationally, time-dependent models that describe both the spatial and temporal variability of seismicity are required. Gathering historic and recent seismicity data, combined with knowledge of seismotectonic properties of a region, allows us to better understand spatial variability in earthquake occurrence in a time-independent manner (Danciu et al., 2021; Crowley et al., 2021; Wiemer et al., 2016). In addition to the time-independent assessment of seismicity, the temporal evolution of seismic sequences can be modelled using well-established empirical laws,

30 as has been done by several (governmental or non-governmental) agencies on various scales (Christophersen et al., 2017; Field et al., 2017; Jordan et al., 2011; Mizrahi et al., 2023b; Marzocchi and Lombardi, 2009; Nandan et al., 2021; Omi et al., 2018).

The main objective of this paper is to develop a harmonized forecasting model for Europe that represents the current state of the art of time-dependent earthquake forecasting. The idea of a harmonized model is to take into account the differences in data collection properties, but also physical properties of various tectonic regions, to minimize the effect of administrative

35 borders on the output, providing a unique set of parameters that, in a way, averages seismicity properties in the observed region, hopefully benefiting from a high variety of events present in such a large dataset. This model is meant to be simple and serve as the basis for the development of future models, and is not meant to overrule other, national forecasting models where they are available (e.g. Italy; Marzocchi et al., 2014). We aim to identify the shortcomings of a basic harmonized model and propose modifications that would remediate them with the goal of providing reliable earthquake probabilities incorporating long-term

40 seismicity rates as well as short-term clustering patterns.

The current state-of-the-art models for time-dependent earthquake forecasting are Epidemic-type aftershock sequence (ETAS) models (Ogata, 1988). Having been introduced by Ogata in 1988, these models have been around for several decades, implemented and used by many agencies and identified by experts in the study of Mizrahi et al. (2023a) as the preferred choice for a default model to be used for earthquake forecasting. Their main strength is in explaining the aftershock triggering behavior

45 of earthquakes, relying on temporal and spatial decay of the number of aftershocks with spatial or temporal distance from the main event, the productivity law, and the Gutenberg–Richter (GR) law (Omori, 1895; Utsu, 1971; Gutenberg and Richter, 1936). In ETAS, the seismicity rate ℓ is given as the sum of the background rate μ and the aftershock rate g of all previous events, following these laws. Specifically, we will use the formulation as in Nandan et al. (2021) and Mizrahi et al. (2021b),

$$\ell(t,x,y) = \mu + \sum_{i:t_i<t} g(m_i, t-t_i, x-x_i, y-y_i), \tag{1}$$

50 $$g(m_i, t-t_i, x-x_i, y-y_i) = \frac{e^{-(t-t_i)/\tau} \cdot k_0 e^{a(m_i-m_c)}}{(t-t_i+c)^{1+\omega}((x-x_i)^2 + (y-y_i)^2 + d e^{\gamma(m-m_c)})^{1+\rho}}.$$

Training such a model for the Europe-wide region poses a number of challenges, as has been laid out by Zechar et al. (2016). A main challenge lies in the compilation of a dataset containing a comprehensive record of earthquakes over a significant period of time, especially considering the differing formats and properties used in different countries or subregions (e.g., magnitude types and their definitions, data completeness due to network density and other reasons, location and magnitude precision,

55 etc.). Moreover, it is desirable to leverage high-quality data (higher precision, completeness to a lower magnitude) where it is available, without losing potentially valuable information about high-magnitude events in periods and regions wherein data

collection was not as precise and complete. Data completeness is often quantitatively expressed through the completeness magnitude (m_c), which is the lowest magnitude above which all events are assumed to be observed. A catalog of all recorded events is normally incomplete, meaning that it also contains events below m_c, and as the exact m_c is not known, it is important

60   to estimate m_c and remove events below m_c. Underestimating it may bias models trained on the data with higher m_c than assumed (Seif et al., 2017), but overestimating it results in throwing away complete and potentially useful data.

Multiple methods for estimating m_c have been developed and tested, mostly relying on the fact that by the Gutenberg–Richter law, the events in a complete catalog follow an exponential distribution, their cumulative count satisfying

$$N(m) = 10^{a-bm}, \tag{2}$$

65   where $N(m)$ denotes the number of events with a magnitude of m and above, and a and b are parameters often referred to as a- and b-value. Note that the natural logarithm base is also used, in which case

$$N(m) = N_0 e^{-\beta m}, \quad N_0 = 10^a, \quad \beta = b \ln 10. \tag{3}$$

Although challenging, recent achievements in data collection and harmonization have enabled the creation of a Europe-wide earthquake catalog which we aim to use as a basis for the calibration of a Europe-wide ETAS model in this study. The main

70   result that will be used in this study in terms of data gathering is the catalog collected for the European seismic hazard model (ESHM20; Danciu et al., 2021), which provides harmonized information about seismic activity on an overall European scale, relying on expert knowledge about the differences in earthquake monitoring and physical tectonic characteristics of the region in order to harmonize the data, and providing elicitation both on data properties (such as m_c) and division into subregions based on their seismotectonic properties. Moreover, the ability to fit ETAS models to datasets with varying m_c introduced by

75   Mizrahi et al. (2021b) allows for ETAS models to use both the high-quality data in (more recent) time periods and sub-regions with low m_c and potentially capture long-term trends contained in periods and areas with higher m_c.

Besides a basic ETAS model, we will consider several modifications and test them both retrospectively for self-consistency and pseudo-prospectively for comparison against one another. While the main strength of ETAS models is in modelling after-shock behavior, it is expected that the background rate varies significantly in space over a large area such as Europe. One of our

80   main proposed modifications focuses on implementing the knowledge about spatial variations in background rate inferred by ESHM20 (Danciu et al., 2021) already during the inversion of ETAS parameters, which could affect the parameters describing aftershock behavior as well. Other modifications include fixing the term dictating the productivity law to the b-value of the catalog (Hainzl et al., 2013; van der Elst et al., 2022) to balance the more productive triggering by high-magnitude events (productivity law; Utsu, 1971) with their much rarer occurrence (Gutenberg–Richter magnitude distribution law; Gutenberg

85   and Richter, 1936) as explained in Helmstetter (2003), and implementing the b-positive method (van der Elst, 2021) for the estimation of the b-value.

The outline of the remaining sections of this article is the following: in Sect. 2, we briefly describe the ESHM20 catalog with both its more recent and historic parts and then describe the selection of the time frame used in this study due to computational limitations and high heterogeneity in data quality among time periods. We introduce additional data about long-term seismicity

90   given by ESHM20 that will be used as input to some model variants and the most recent catalog that will be used for model validation. The development of a base model and modifications thereof are described in more detail in Sect. 3, followed by a description of the methods used for testing them (Sect. 3.3 and 3.4). Finally, our results are presented and discussed in Sect. 4, divided into three parts, presenting the fitted parameters of the models, results of retrospective consistency tests, and results of pseudo-prospective model comparison experiments.

2   Data

95

The primary dataset used in this work is the ESHM20 catalog (Danciu et al., 2021), which contains the combined catalogs of all agencies that record earthquakes in Europe, both recent and historical, dating back to the 11th century. Due to the variations in both the nature of earthquake occurrence and its monitoring, the data are highly heterogeneous. For pre-instrumental times, the records are highly incomplete, potentially missing even the high-magnitude events and the magnitudes of the events that

100   are in the record containing errors potentially higher than 0.5 magnitude units (Grünthal et al., 2009; Grünthal and Wahlström, 2012). As the density and sensitivity of seismic networks generally improve over time, the magnitude and location precision increases (Danciu et al., 2021), as well as the number of recorded events due to the ability to record lower-magnitude events (the completeness magnitude m_c decreases). However, neither the level of completeness nor this improvement over time are spatially uniform. Between some regions, in the same period, m_c difference can be up to four magnitude units. Although a

105   more precise magnitude resolution is available for a part of the data, the agreed-on precision is 0.2, as in Danciu et al. (2021).

Due to computational limitations, poor quality, and strong incompleteness of early data, which make it unsuitable for the analysis of aftershock behavior, the dataset needs to be narrowed down to contain relatively recent information while ensuring a sufficiently long time frame that enables the capturing of longer-term triggering effects and seismicity patterns. High-magnitude events that are present in historical parts of the catalog are crucial to better understand the frequency of rare seismic events

110   that are not present in more recent time periods, and they help to identify additional spatial patterns in background seismicity. However, these historical high-magnitude events will seldom have aftershocks recorded due to the incompleteness reflected in m_c going as high as magnitude 8. Up to the early 1980s, the highest completeness difference between regions in the same time period is as high as three magnitude units; starting from the 1990s, this difference lowers to 1.5 units of magnitude. Hence, we here limit the catalog to the time period starting with the year 1980, with only events after 1990 considered as potentially

115   triggered events (this is discussed in more detail later, in Sect. 3.2.1). The spatial distribution of the catalog containing over 20 thousand events in this time period is shown in Fig. 1(a) (in red). While the aforementioned issues of earthquake monitoring in earlier parts of the catalogs are fewer in the selected recent time period, the effect of neglecting to address them (such as assuming a too low m_c or too high magnitude precision) could still potentially significantly bias our later output (Seif et al., 2017).

120   By definition of the completeness magnitude, all events of magnitude equal to or higher than m_c are assumed to be recorded. The events of magnitude below m_c are also present in the raw catalog, resulting in incompleteness in the data. The incompleteness in this dataset below magnitude 4.6 is so evident that it is detectable already through visual inspection of Fig. 1(b–c).
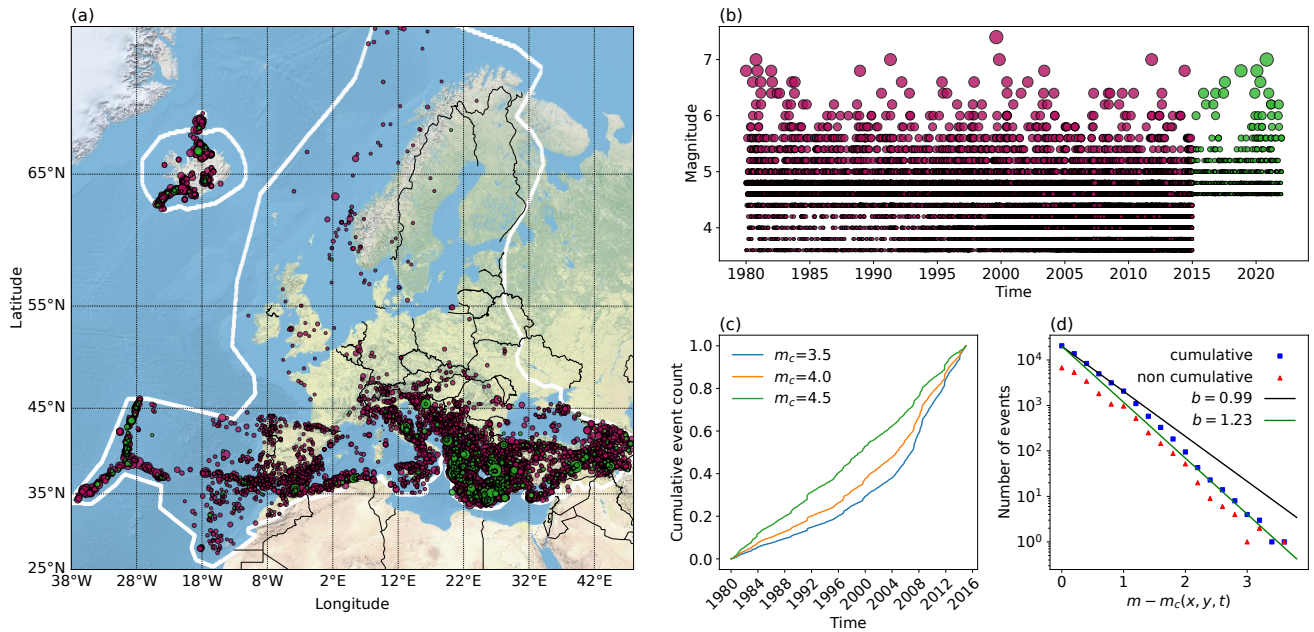
Figure 1. Dataset used for model training (1980–2015, red dots) and testing (2015–2022, green dots); in (c–d) only the training dataset is shown. (a) Map of events detected in the study area defined in ESHM20. The dot size increases with magnitude. (b) Time evolution of recorded events' magnitudes. The dot size increases with magnitude. (c) Cumulative count of recorded events through time for different cutoff magnitudes. (d) Magnitude frequency distribution plot. The distribution of $m - m_c(x, y, t)$ is shown to correct for varying completeness.

Namely, under the assumption that the observed number of events does not have a significant trend over a longer period of time, the cumulative count of events through time would display a roughly linear increasing behavior, with rapid jumps in the count at a point indicating only the occurrence of a productive sequence of events. The changes in the slope of this linear increase shown in (c) indicate the changing completeness over that time period and an increase in the rate of cumulative earthquake count, suggesting that completeness improves over time. In (b), both incompleteness and discretisation are discernible in the plot showing recorded magnitudes over time.

The study of Danciu et al. (2021) provides expert evaluations of the completeness magnitudes by region and time period. Knowing these m_c values allows accounting for the incompleteness of data later during model calibration as described in Mizrahi et al. (2021b). As m_c differs between regions and time periods, the distribution of $m - m_c(x, y, t)$ is shown in Fig. 1(d) instead of a distribution of "pure" magnitudes to correct each magnitude for the corresponding incompleteness level.

The catalog of Danciu et al. (2021) ends in 2015 and we use it in full for model training. The continuation of the catalog is given in Lammers et al. (2023) until 2022 and this seven-year period is used here for pseudo-prospective testing. This new part of the catalog is not identical in composition to the catalog used for training, the most prominent difference being the completeness magnitude of 4.6 in the overall dataset (demonstrated in Fig. 1(b)). The spatial distribution of the testing catalog is shown in Fig. 1(a) (in green). In truly prospective testing, such differences are not only possible, but an expected occurrence,

the effect of which is not to be disregarded, but rather leveraged to obtain more robust models. Note that in both the training and testing catalog, due to the binning of $\Delta m = 0.2$ mentioned above, a completeness magnitude m_c means that it actually contains events above $m_c - 0.5\Delta m = m_c - 0.1$.

Furthermore, in this study, alongside earthquake catalogs, we aim to utilize the long-term seismicity rates introduced by Danciu et al. (2021). These rates are provided for both the area sources model and the background seismicity and active faults model. The area sources model is a classical seismogenic source model, describing seismicity as shallow crustal, volcanic, subduction in-slab and deep, relying on recommendations by regional and national experts with modifications made to ensure compatibility in bordering (overlapping) areas. The background seismicity and active faults model combines the smoothed background seismicity model obtained by estimating activity parameters (a- and b-value in the GR law) on a declustered complete catalog and the model describing seismic productivity in the proximity of faults with a fault-dependent magnitude threshold between them ensuring avoiding double counting seismicity. As in ESHM20, the annual seismicity rates for each spatial and magnitude bin are obtained by combining the outputs of these two models, with equal weighting. Summing the rates across all magnitude bins and accounting for differences in completeness magnitude and time duration yields overall daily background seismicity rates for the spatial bins defined in the study. By adding this extra input, we include information from the historical periods of the ESHM catalog about large events and seismicity in areas not represented in the selected training part of the catalog (after 1980).

3 Methods

3.1 ETAS

Training an ETAS model on a given dataset means finding the parameters in (1) that give the best fit to the data. The inversion of the ETAS parameters μ, k_0, a, c, ω, τ, d, ρ and γ used here is based on an expectation–maximization (EM) algorithm (Veen and Schoenberg, 2008), with the varying m_c adjustment (Mizrahi et al., 2021b). Conservatively using the maximum value of m_c across the entire catalog would result in the loss of a large amount of valuable data, while assuming a completeness magnitude lower than the true one could introduce biases to our calculations (Seif et al., 2017).

In this modified EM algorithm by Mizrahi et al. (2021b), the difference between the overall lowest completeness magnitude, m_{ref}, and the completeness magnitude at the location and time of a given event, $m_c(x, y, t)$, is taken into account for each event by estimating the ratio of the unobserved and observed events (ζ), and the ratio of events triggered by unobserved and observed events (ξ) based on the Gutenberg–Richter magnitude distribution assumption. The algorithm has been implemented in Python by Mizrahi et al. (2023c) and can, in principle, be used to calibrate basic ETAS models on any given catalog.

As the computation of ζ and ξ relies on the GR law to estimate the number of unobserved events, this method is dependent on the estimated b-value of the catalog. Therefore, we test both the classical maximum likelihood method with adjusting for binning described in Tinti and Mulargia (1987), and the b-positive method (van der Elst, 2021) which is meant to overcome incompleteness in data, primarily the short-term aftershock incompleteness (STAI; Kagan, 2004).

170   In an ETAS model which produces a unique set of parameters for the overall region, information and properties of specific
faults and sequences are potentially lost, but the advantage of global models is in their training datasets containing a larger num-
ber of high-magnitude earthquakes (Bayona et al., 2023). Another approach for mitigating the averaging behavior of a global
model is to update the aftershock behavior described by ETAS with real-time data from an ongoing sequence when issuing
aftershocks forecast operationally (Omi et al., 2015; van der Elst et al., 2022). The implementation of such a sequence-specific
175   model updating, however, still involves a number of expert decisions, and there is no substantial evidence in favor of a unique
updating approach that would improve the overall performance of a global model. While this is a feasible direction for future
European model development, here we focus on developing a baseline, harmonized model upon which such improvements
could be built.

3.2 Model variants

180   In addition to fitting an overall generic ETAS model to our dataset, in this section we propose modifications that could, in
principle, be applied to any ETAS model. The models compared in this study are as follows.

  – ETAS_0: A basic ETAS model - set of parameters fitted to the ESHM20 dataset with no additional input or constraints.
    The implementation relies on the EM algorithm (Veen and Schoenberg, 2008) with varying m_c modification (Mizrahi
    et al., 2021b).

185   – ETAS_{bg}: In order to be consistent with the long-term model (ESHM20; Danciu et al., 2021) and to utilize the information
    contained in the hazard model about spatially varying seismicity rates, the parameter inversion algorithm is modified to
    allow for variations in the background rate.

  – ETAS_α: Due to the observed behavior of ETAS models to underestimate the productivity of high-magnitude events, the
    parameter dictating the productivity law $\alpha = a - \rho\gamma$ is fixed to $\alpha = \beta$ as a constraint during inversion.

190   – $\text{ETAS}_{\text{bg}, \alpha}$: The two proposed modifications are combined.

  – $\text{ETAS}_0{}^{b+}$, $\text{ETAS}_{\text{bg}}{}^{b+}$, $\text{ETAS}_\alpha{}^{b+}$, $\text{ETAS}_{\text{bg}, \alpha}{}^{b+}$: The four model variants introduced above, the only difference being in
    the b-value estimation method (van der Elst, 2021).

  – $\text{ETAS}_{\text{USGS}}$: To add a comparison level and check for the benefits of fitting an ETAS model specific to European data, we
    use the parameters from the prior models described in van der Elst et al. (2022), applied by the USGS AftershockFore-
195   caster software.

  – Poisson background model: We implement a time-independent model that takes the seismicity rate map provided by
    ESHM20 (Danciu et al., 2021) and, for each spatial cell in this map, forecasts a number of events following the Poissonian
    distribution with the corresponding rate in that cell as a mean. This is the null model against which comparisons are made
    in the testing phase to check for the performance of added time-dependent information during aftershock sequences.

3.2.1 ETAS$_0$, ETAS$_0{}^{b+}$

These two models are trained using the general ETAS method, as introduced in Sect. 3.1, on the ESHM20 catalog filtered as described in Sect. 2. Although the full training period includes data between 1980 and 2015, the first ten years are used as a "burn period" - these events are interpreted as potentially triggering events, but we do not consider them as possible aftershocks of previous earthquakes. Without this "buffer" time period, the events near the beginning of the selected time window would all be interpreted as background events, having no preceding seismic activity acting as their potential triggering events. Additionally, this same auxiliary period will be used when simulating catalogs for purposes of retrospective consistency testing, since in the simulated catalogs starting in 1990, we need both background events and aftershocks of seismicity that occurred prior to 1990.

Having a unique set of parameters for the entire Europe provides a harmonized model that describes the aftershock behavior in the region. For each event, the EM parameter inversion algorithm also yields the probability that it is a background or a triggered event. This allows us to capture the spatial variations in rates of background events despite the fact that the background parameter μ is treated as a constant during the parameter inversion. When simulating catalogs that are later used for producing retrospective and pseudo-prospective forecasts, we use this background rate information by drawing the events' locations based on the probabilities that each observed event in the training catalog is a background event.

3.2.2 ETAS$_{bg}$, ETAS$_{bg}{}^{b+}$

We mentioned in Sect. 3.2.1 that the probabilistic branching structure inferred during the parameter inversion stage can be used to simulate new catalogs that will be consistent with the observed background event rates at different locations. However, a desired property of our model would be the ability to include the knowledge about variation in the background rate already during the parameter inversion, in order to estimate the background probabilities of events more correctly, and also to achieve consistency of the background seismicity rates with the ones in the long-term hazard model (Danciu et al., 2021). This means that the time-independent seismicity rates provided by the hazard model should match the time-dependent ones when computed over very long periods of time. For this reason, the model is adjusted to allow for the now space-varying background rate:

$$\ell(t,x,y) = \mu(x,y) + \sum_{i:t_i<t} g(m_i, t-t_i, x-x_i, y-y_i), \tag{4}$$

similar to the ETAS formulation with an inhomogeneous background rate $\mu(x,y)$ suggested in Veen and Schoenberg (2008), where μ is modelled by subdividing the spatial observation window into n cells with constant background rate μ_k, $k = 1, \ldots n$. Here, we allow for the variation between different locations to be fixed to the levels given as input to the ETAS parameter inversion. More precisely, during the expectation step in the calculation of the probability that one event triggered another one, the term μ representing the background contribution is replaced with

$$\mu(x,y) = \iota \cdot \mu_k, \tag{5}$$

230 where ι is a parameter learned in the inversion, estimated in every iteration as the total number of background events in the entire area, normalized per day and km^2, and μ_k is the long-term annual seismicity rate given as an input corresponding to the cell that contains the location (x, y). The probability that event i triggered event j estimated in the $(n+1)^{\text{th}}$ iteration is then given as

$$P^{(n+1)}(i \to j) = \frac{g(m_i, t_j - t_i, x_j - x_i, y_j - y_i | \theta^{(n)})}{\iota \cdot \mu_{k:j \in \text{cell } k} + \sum_{i:t_i < t_j} g(m_i, t_j - t_i, x_j - x_i, y_j - y_i | \theta^{(n)})}, \tag{6}$$

235 where $\mu_{k:j \in \text{cell } k}$ is the long-term annual seismicity rate given as an input corresponding to the cell that contains the location (x_j, y_j).

As ι is estimated in each iteration as the total estimated number of background events per day and km^2, it represents the overall background rate. Therefore, the information that needs to be taken from the input background level is not the absolute background rate in the corresponding spatial cell, normalized per time and area unit, since multiplying two such values would
240 result in a quick convergence of this parameter to zero. Rather than that, we only take the relative relationship between these rates among different spatial cells by normalizing the values μ_k before inversion so that $\frac{1}{n} \sum_{k=1}^{n} \mu_k = 1$, where n is the number of $0.1° \times 0.1°$ cells that cover the area of interest, in our case $n \approx 8 \cdot 10^5$. For each event in the catalog, we assign the corresponding background seismicity level within its respective bin, which is then used as μ_k during the inversion.

3.2.3 ETAS$_\alpha$, ETAS$_\alpha{}^{b+}$

245 In the literature, it has been observed that there is a tendency in ETAS models to underestimate the productivity of large events (Hainzl et al., 2013) due to their under-representation in training data. Therefore, another proposed modification of the model is to allow the productivity term $\alpha = a - \rho \cdot \gamma$ to be fixed to a given constant. This term emerges from our ETAS formulation as the exponent in the relationship between the magnitude of an event and its expected number of aftershocks.

While the productivity law describes an increase in the number of aftershocks with the magnitude of the main event, the
250 GR law describes that there are relatively fewer large than small magnitude events. As described in Helmstetter (2003), the relationship between the two exponents of these exponential relationships, α and β, determines whether earthquake triggering is driven by small or large magnitude events - and stipulating that $\alpha = \beta$ balances the influence of events of different magnitudes in earthquake triggering.

In the ETAS$_\alpha$ model variant, we apply this fixed α during the inversion based on the EM algorithm, which naturally affects
255 all parameters. For this modification of the ETAS model, we set $\alpha = \beta$, as suggested in van der Elst et al. (2022) when $b < 1$, where β is the GR parameter. When estimating the b-value with the b-positive method (van der Elst, 2021) for the ETAS$_\alpha{}^{b+}$ model variant, we obtain $b > 1$. Therefore, following the recommendation by van der Elst et al. (2022), in order to prevent the "exploding" behavior of aftershock triggering, we fix the productivity term to $\alpha = e$.

3.2.4 ETAS$_{USGS}$

260 The prior models used by the USGS AftershockForecaster software are fitted separately for different tectonic regimes, hence, more than one set of parameters exists. The sequences in the European dataset originate from various tectonic regimes, therefore we use their "global average" set of parameters. These parameters are expressed in the standard ETAS formulation, where the temporal decay is given as $(\Delta t + c)^{-p}$, as opposed to the formulation in Eq. (1) used here, where the temporal decay is described by the factor $(\Delta t + c)^{-(1+\omega)} \cdot e^{-\Delta t / \tau}$. The productivity law in the standard formulation is expressed as $10^{-\alpha(m_i - m_c)}$,

265 where m_i is the magnitude of the triggering event, and in Eq. (1), it is given as $k_0 e^{a(m_i - m_c)}$, but also influenced by the spatial kernel term $\left(\Delta x^2 + de^{\gamma(m - m_c)}\right)^{-(1+\rho)}$. As no spatial parameters are specified in the parameter set given in the Aftershock-Forecaster software documentation, we use the spatial kernel inverted by ETAS$_0$. Additionally, we use μ and the background locations inferred by ETAS$_0$ because the USGS models are fitted only to aftershock sequences and do not account for background seismicity. Keeping in mind the different m_c, which in the USGS global average parameter set is 4.5, we translate the

270 parameters into our formulation as in Mizrahi et al. (2023b). Note that our version of the model is a simplification of the actual model employed by the USGS AftershockForecaster software and is not meant to replicate it exactly; the aim of including the model in our study is solely to assess the usefulness of locally calibrated parameters compared to globally calibrated ones.

3.3 Consistency testing

A basic set of tests that one can do to assess the consistency of the models with past data is defined by The Collaboratory for the

275 Study of Earthquake Predictability (CSEP; Savran et al., 2020; Zechar et al., 2010). Passing retrospective number, magnitude, space, and pseudo-likelihood tests would imply that a model forecasts the occurrence of a similar number of similar magnitude events at places where they were observed in the training data.

Based on the background event occurrence and aftershock triggering laws inferred during the inversion of ETAS parameters, we simulate 100k synthetic catalogs for the training period (1980–2015). The simulation procedure has been implemented in

280 Mizrahi et al. (2023c) following the detailed description in Mizrahi et al. (2021b) and accounts for higher-order aftershocks. First, the background events are simulated by drawing their count from a Poisson distribution with the mean corresponding to μ, occurrence time from a uniform distribution, and magnitude from a GR distribution (β estimated from the data). For models with no additional background information given as input, the locations of the background events are drawn from the locations of existing events, weighted by their probabilities of being background events. For models with informed background

285 introduced in Sect. 3.2.2, the same background input which is used during inversion is also used as the spatial distribution of simulated background events.

The first generation of aftershocks is simulated by generating aftershocks of all events in the "starting" generation - their number, location, timing and magnitude are determined by the productivity law, spatial decay, temporal decay and GR law, respectively. Further generations of aftershocks are simulated iteratively by simulating aftershocks of all events in all previous

290 generations until the number of events in the new generation becomes zero. Here, the auxiliary "burn" period (see Sect. 3.2.1) from 1980 to 1990 of the true catalog is used together with a set of simulated background events between 1990 and 2015 as

a starting generation of events. For all models, the maximum magnitude during the simulation phase is set to $m_{\mathrm{max}} = 10.0$, which, due to the binning value of $\Delta m = 0.2$ corresponds to $m_{\mathrm{max}} = 10.1$.

The number test (N-test) consists of counting the number of events in each catalog to get an approximation of the distribution

295 of the forecasted number of events, which is then checked against the observed number of events in the true catalog. The quantile score of the test is computed as the probability of observing the true number of events under the assumption that the number of events follows the distribution approximated by the simulations. This hypothesis is then rejected when the quantile score is below 0.05 or above 0.95 (extreme 10% of the forecasted distribution).

Similarly, the magnitude test (M-test) and the space test (S-test) compare the number of observed and forecasted events

300 taking into account their magnitudes and locations, respectively. In the magnitude test, the distribution of deviations of each simulation's magnitude distribution from a "theoretical" magnitude distribution described by the set of all events across all simulations is compared to the same deviation for the magnitude distribution in the true catalog. This deviation is calculated as the sum of squared logarithmic residuals between the normalized observed magnitudes and the "theoretical" magnitudes' histogram.

305 In both spatial and pseudo-likelihood tests, the property of interest in the simulated catalogs and the true catalog is not their length (as in the N-test) nor a metric describing the deviation of a magnitude distribution from the theoretical one (as in D*-statistic for the M-test), but pseudo-likelihood computed as the sum of the approximate rate density over all spatial bins. The pseudo-likelihood test combines space-magnitude gridding to obtain an overall comparison of the consistency between forecasted and observed catalogs. Unlike the number test, these tests are defined as one-sided, meaning that the hypothesis that

310 the true magnitude or spatial distribution follows the one in simulations is only rejected when the quantile score is above 0.9 in M-test or below 0.1 in S-test and PL-test.

Due to the varying completeness magnitude, each event is given a weight during the inversion of ETAS parameters correcting for the estimated number of unobserved events at the time and location of that event. The simulated catalogs contain events above m_{ref}, the minimum m_c across the entire catalog, while the true catalog only contains the events above the corresponding

315 $m_c(x, y, t)$. To make the synthetic catalogs comparable with the true catalog, we are cutting off the synthetic catalogs to only contain events above the corresponding $m_c(x, y, t)$ values.

While the same tests can be performed pseudo-prospectively, meaning with test data that the model was not trained on (in our case, that is the data after 2015), to check for consistency with the training data, we focus on performing the tests retrospectively. Apart from providing a sanity check and indicating potential shortcomings of a model, retrospective consistency testing enables

320 evaluating its performance on long-term data, which is not available in the post-training time period (in our case seven years, versus the 35-year-long training period). These tests are performed on each model separately.

3.4 Pseudo-prospective testing

To compare the performance of the models in terms of their forecasting power, we set up a pseudo-prospective forecasting experiment. Each model is used to simulate 100,000 synthetic catalogs for consecutive one-day testing windows in the seven-

325 year-long testing period. The simulations are created similarly to the procedure described in Sect. 3.3, with the starting set

of events consisting of the full training catalog and the portion of the testing catalog up to the time window for which the forecast is made. The aftershocks of all these events are then simulated based on the modelled aftershock behavior to create the first generation of aftershocks, and further generations are simulated iteratively until convergence. For each time window, the corresponding simulations are used to find a distribution of the number of events in each spatial bin.

330   Having estimated the forecasted distribution of the number of events in each spatial bin ($j = 1, \ldots, N$) for every time window (indexed with i), the forecast can now be compared to reality by checking the probability of the true number of events in that space-time bin ($n_{i,j}$) given by the estimated distribution. This is done for each spatial bin, and then summed over all spatial bins resulting in the log-likelihood score of a model for a forecasting time horizon given as in Nandan et al. (2019) and Nandan et al. (2022):

$$\mathcal{LL}_{\text{model}}^i = \sum_{j=1}^{N} \ln\left(P_{\text{model}}^i(n_{i,j})\right). \tag{7}$$

     Note that when the estimated probability of k events occurring in a spatial bin is zero, this log-likelihood score would not be well defined. For this reason, after simulating the synthetic catalogs and observing the distribution of the number of events in each spatial cell, we slightly alter this distribution by assigning a small probability ($\sim 10^{-7}$) to the bins (up to a maximum bin $n_{\max}$) with a zero count, adjusting the event counts in all other bins to retain the property that the sum of probabilities of all event counts is 1.

     Within this experiment, the spatial bins are set to $0.1°$ lon $\times$ $0.1°$ lat, the time window to 1 day, and events with magnitudes 4.6 and above are considered, which is the generally valid completeness magnitude in the testing part of the catalog. Since the experiment is pseudo-prospective, the new part of the catalog is available and seven years of data since 2015 can be used for validation and testing, resulting in 2558 testing windows for which each model produces 100k synthetic catalogs.

345   As mentioned earlier, the baseline against which all model variants are tested is the Poisson background model, for which generating synthetic catalogs is not needed. Within each spatial cell, the number of events is considered to follow a Poisson distribution with mean $\lambda_j = \mu_{j,\text{ESHM}}$, where $\mu_{j,\text{ESHM}}$ is the daily seismicity rate in the jth spatial cell given by ESHM20. The log-likelihood in Eq. (7) becomes

$$\mathcal{LL}_{\text{ESHM20}}^i = \sum_{j=1}^{N} \ln\left(P_{\text{ESHM20}}^i(n_{i,j})\right) = \sum_{j=1}^{N} \ln \frac{\lambda_j^{n_j} e^{-\lambda_j}}{n_j!}, \quad \text{for every time window } i. \tag{8}$$

350   The metric used for comparison of the models is simply the difference between their log-likelihood scores, called the information gain (IG). For each time window, we have a value of IG of one model over another, and while the cumulative information gain is indicative of models' performance through time, we test whether one model outperforms another by testing whether the mean information gain (MIG) between that pair of models is significantly positive using a paired one-sided t-test.

4 Results and Discussion

4.1 Model fit

As mentioned in Sect. 3, fitting an ETAS model to the data means finding a unique set of parameters describing the observed aftershock triggering behavior. The set of inverted parameters for each of the described ETAS model variants is given in Table 1. The parameter μ describes the overall rate of background events and it is estimated by counting the total number of background events and normalising it per day and km^2. The count of background events is obtained by summing the probabilities p_{BG} that are assigned to each event during the parameter inversion, weighted by the estimated ratio of unobserved and observed events ζ introduced in Sect. 3.1 to account for incompleteness.

As the parameters can be grouped into those describing temporal decay, spatial decay and productivity law, the curves of each can be plotted separately as in Fig. 2. These curves represent the modelled aftershock triggering behavior and are compared to the observed aftershock triggering behavior in the true catalog, represented by dots. However, since the true triggering relationship between events in the true catalog is unknown, for counting aftershocks triggered by an event of a certain magnitude at a given temporal and spatial distance, we rely on the probabilistic triggering structure inferred during the expectation step of the EM algorithm. Therefore, the observed aftershock triggering behavior is, in fact, dependent on the inverted triggering parameters.

In Fig. 2(a), the curves show the temporal decay in aftershock behavior described in ETAS as

$$N(\Delta t) = \frac{\exp(-\Delta t/\tau)}{(\Delta t + c)^{(1+\omega)}}, \tag{9}$$

and the dots represent the "observed" aftershock behavior by showing counts of pairs of events (i,j) where i triggered j with probability p_{ij} and $\Delta t = t_j - t_i$, computed as $\sum_j p_{ij} \cdot \zeta(j)$. In the top row, the different curves represent triggering laws that were inferred on different datasets: the European catalog used in the present study, Swiss seismicity (Mizrahi et al., 2023b), Californian seismicity (Mizrahi et al., 2021a), and parameters used by the USGS AftershockForecaster software (spatial kernel is taken from ETAS_0 as mentioned in 3.2.4); in the bottom row, the different curves represent the laws inferred by different ETAS variants. In a similar fashion, the spatial decay depicted in Fig. 2(b) shows the number of triggered aftershocks at distance Δx described in the ETAS model as

$$N(\Delta x) = ((\Delta x)^2 + d \exp(\gamma(m - m_c)))^{-(1+\rho)}. \tag{10}$$

As there is a dependency in the spatial decay on the magnitude, there is a curve describing this law for each magnitude bin. In Fig. 2(b), we show $m = 4.0$. The line in Fig. 2(c) shows the dependency of the number of triggered events on the magnitude of the triggering event, described in ETAS formulation with the productivity law,

$$N(m) = k_0 \exp(a(m - m_c)). \tag{11}$$

Table 1. Inverted ETAS parameters for each of the eight ETAS variants described in Sect. 3. Additional parameters include the b-value, productivity term $\alpha = a - \rho\gamma$ and the branching ratio η.

Model	ETAS_0	ETAS_α	$\mathrm{ETAS}_\mathrm{bg}$	$\mathrm{ETAS}_{\alpha,\,\mathrm{bg}}$	$\mathrm{ETAS}_0{}^{b+}$	$\mathrm{ETAS}_\alpha{}^{b+}$	$\mathrm{ETAS}_\mathrm{bg}{}^{b+}$	$\mathrm{ETAS}_{\alpha,\,\mathrm{bg}}{}^{b+}$	$\mathrm{ETAS}_\mathrm{USGS}$
$\log_{10}\mu$	-7.94	-8.08	-7.24^{a}	-7.22^{a}	-7.75	-7.98	-7.05^{a}	-7.01^{a}	-7.94
$\log_{10}k_0$	-1.63	-2.51	-1.40	-2.07	-1.63	-2.96	-1.39	-2.34	-2.63
a	1.59	3.11	1.79	3.27	1.68	3.70	2.05	3.93	2.87
$\log_{10}c$	-2.65	-3.01	-2.37	-2.43	-2.58	-3.22	-2.27	-2.39	-2.57
ω	-0.11	-0.15	-0.04	-0.05	-0.10	-0.18	-0.02	-0.04	-0.03
$\log_{10}\tau$	3.66	3.9	3.44	3.78	3.67	3.98	3.46	3.89	12.26
$\log_{10}d$	0.92	0.54	0.90	0.69	0.90	0.30	0.86	0.60	0.92
ρ	0.61	0.55	0.81	0.82	0.64	0.54	0.87	0.90	0.61
γ	0.92	1.52	0.88	1.20	0.94	1.81	0.96	1.35	0.92
b	0.99	0.99	0.99	0.99	1.23	1.23	1.23	1.23	1
α	1.03	2.28	1.08	2.28	1.08	2.72	1.21	2.72	2.28
η	1.00	4.46	0.75	3.03	0.83	1.78	0.60	1.12	4.04

[a] Spatially varying, showing the approximated average (ι in Eq. (5)).

Discussion of the model fit

Comparing multiple models trained on the European dataset based on the ETAS parameters shown in Table 1, we consistently observe that the background term μ is higher in models that allow for background term variation during the inversion. This is in agreement with the idea that using an informed background term μ during inversion allows models to recognize more events in active areas as background events, while they would be interpreted as triggered events (triggered by other events in the same active area) without the added background information. That more events are interpreted as background events rather than aftershocks also manifests in the fact that informed-background model variants have lower overall productivity. This is seen in the branching ratio η, which reflects the average number of aftershocks per triggering event, being lower for the background-informed models when compared to their constant-background counterparts. Furthermore, the lines in Fig. 2(c), second row are almost parallel in between informed and non-informed background versions of the same model variants, but the line describing the informed background variant is always below the line for the corresponding model with no informed background.

While the background-informed model variants have overall lower productivity than their equivalents with no background information used during the inversion, another, more obvious, difference in the productivity law is seen between the corresponding models with and without fixed α term. Fixing this parameter to the GR β value directly affects the productivity law plot as the slope of the lines is exactly α, resulting in a steeper slope which indicates relatively higher productivity assigned to high-magnitude triggering events compared to low-magnitude triggering events. Fixing α also drastically increases
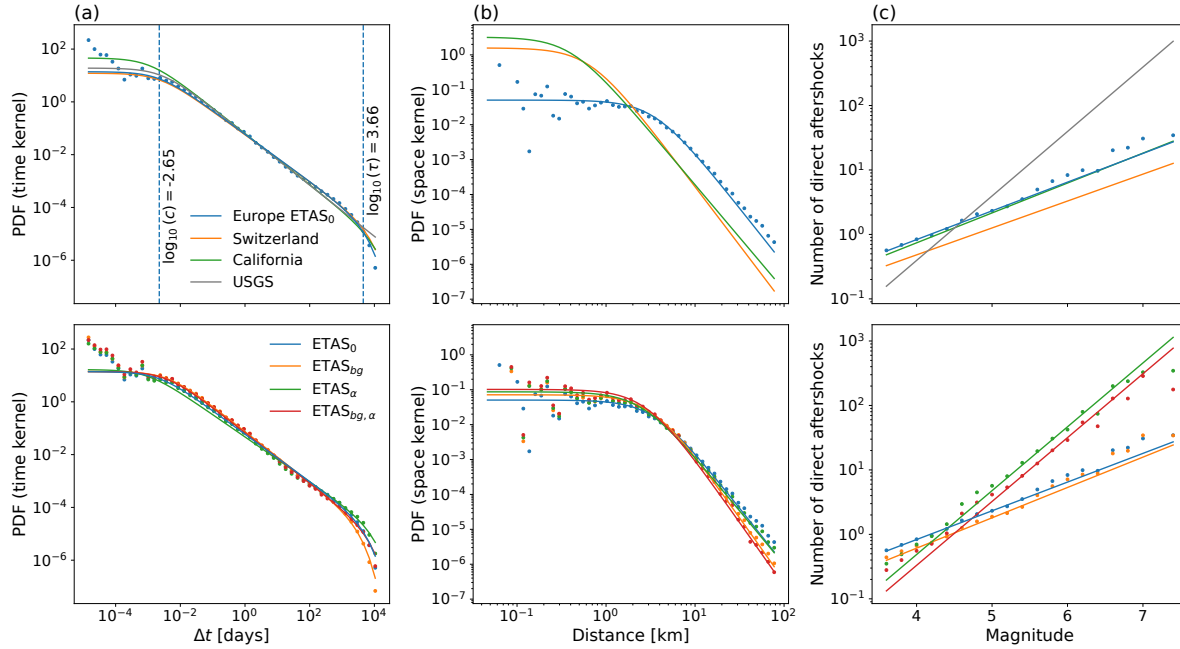
Figure 2. Plots of the model fit. In the first row, triggering laws inferred with model ETAS$_0$ are shown, including lines representing models for other areas for comparison. In the second row, modifications introduced in Sect. 3.2 are compared. (a) Temporal decay. (b) Spatial decay. Due to the dependency of the spatial decay law on the magnitude of the triggering event, there is a curve describing this law for every magnitude, here $m = 4.0$. (c) Productivity law.

the branching ratio η. In non-informed background model variants, this increase in productivity is counterbalanced with a lower background rate. Interestingly, the informed background model variants show increased productivity and increased background rate when α is fixed.

Furthermore, model variants relying on the b-positive estimate of the b-value consistently display a higher background seismicity level and lower overall productivity, but higher productivity term α than their counterparts using the traditional b-value estimator. All these differences must be due to what the model infers about unobserved events below $m_c(x,y,t)$ from the observed ones by applying the GR law. A higher b-value leads to a larger number of expected unobserved aftershocks of observed events. Thus, when $m_c(x,y,t) > m_{\text{ref}}$, the observed large-magnitude events' productivity is inflated, while smaller-magnitude events' productivity is not (or less) inflated, explaining the larger α for b-positive variants. The higher background rate and lower branching ratio of b-positive variants suggest that the parts of the catalog that are less complete, hence more inflated when the b-value is high, exhibit this behavior. To decide whether this is caused by differently behaving seismicity in certain areas or time periods, or whether this indicates that seismicity behaves differently for larger magnitude events compared to smaller ones, further research is required.

Apart from differences among models in interpreting events as background or triggered, a trend in some of the other parameters can also be observed. In the spatial distribution of aftershocks, models with fixed productivity tend to have higher γ, but
415 lower d values, interpreting more of the events at smaller distances as aftershocks of low-magnitude events and more of events further away as aftershocks of large-magnitude events. For the temporal distribution of aftershocks, the higher ω in background-informed models implies a slower decay of the number of aftershocks, whereas the fixed productivity variants have lower ω values, resulting in a faster decay. However, τ is larger for fixed productivity variants and lower for background-informed variants, meaning that the tapering of the distribution will occur later in the former case and sooner in the latter.

420 When comparing the laws described by ETAS models' parameters, we observe differences not only among model variants introduced in our study but also among models calibrated on distinct datasets. While the time kernels appear quite similar across models for different regions, including multiple "European" models, a notable disparity arises in the spatial kernel when comparing the European models to those trained for Switzerland (Mizrahi et al., 2023b) or California (Mizrahi et al., 2021a), as can be seen in Fig. 2(b), first row. Specifically, we note a lower frequency of observed aftershocks at shorter distances
425 from the triggering event, with a subsequent decay starting at slightly greater distances. Since we observe this difference when comparing to models calibrated on other datasets, but not when comparing multiple European models, one possible explanation for this observation could be differences in location determination of events, due to lower location precision and possible short-term incompleteness (close in time and space to triggering events) in some areas in this highly heterogeneous catalog. This idea is supported by the fact that the difference between spatial kernels diminishes with an increase in the magnitude of the
430 triggering event.

Additionally, the comparison between the ETAS variants fitted to the European dataset and the adjusted ETAS parameters used by the USGS AftershockForecaster software reveals that the productivity law is more similar to those inferred by ETAS variants with fixed α, which is expected given that α is fixed to 1 (log-base 10, in our formulation this corresponds to $\alpha = e$) in all sets of parameters used by USGS models. Another difference is in the temporal kernel, which in the case of ETAS$_{\text{USGS}}$ does
435 not have a tapered exponential form. This results in relatively more aftershocks forecasted in periods long after the triggering event; in Table 1, all models have a τ value between 10^3 and 10^4, whereas in ETAS$_{\text{USGS}}$, it is set to 10^{12}, corresponding to a period of 5 billion years (effectively, this means there is no taper).

4.2 Results of consistency tests

To visualize the output of CSEP consistency tests, the PyCSEP implementation Savran et al. (2022) provides the option to
440 display the modelled behavior of the events as a histogram created based on the set of a large number of synthetic catalogs given as the output of a model (catalog-based forecast), and compare it to the true value in the observed catalog represented by a dashed vertical line.

In our case, the distribution of the number of events is approximated by counting the lengths of all simulated catalogs and the vertical line is the size of the catalog which was used in training for the inversion of ETAS parameters. Figure 3(a) shows
445 the visualization of the N-test for ETAS$_0$, the histogram describing the model's distribution of the number of events, whereas the vertical line represents the number of events in the true catalog.
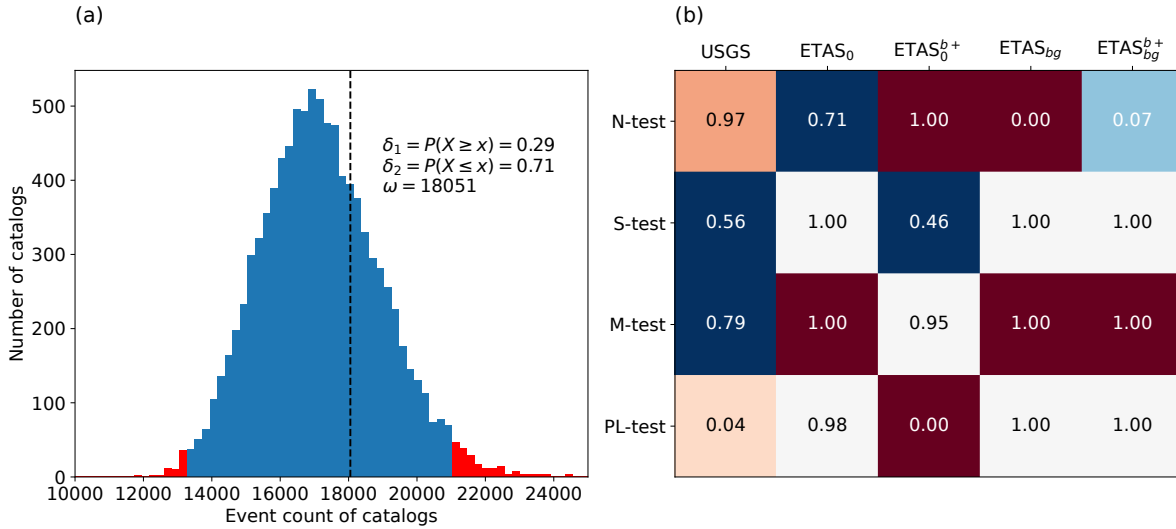
Figure 3. (a) The number test (N-test) for $ETAS_0$: histogram represents the modelled distribution of the number of events approximated by the counts of events in 10k simulated catalogs with completeness levels as in the training catalog. (b) The table contains the quantile score of models introduced in Sect. 3 for each of the consistency tests.

The quantile scores for all tests and all model variants that do not fix α are shown in Fig. 3(b) and represent the position of the dashed line showing the observed property with regards to its forecasted value shown by the histogram (see Fig. 3(a)). Quantile scores between 0.05 and 0.95 indicate that the N-test is passed, while values below 0.05 or above 0.95 indicate that a

450   model has failed the test. In case of S-test and PL-test, the tests are one-sided, therefore, the models with quantile scores above 0.1 pass the tests. M-test is also one-sided, but defined so that the models with quantile scores below 0.9 pass the test.

Discussion of the consistency test results

Due to the large branching ratio $\eta > 1$ in all ETAS variants with fixed productivity term α, the number of events quickly explodes when simulating over a long-term period, as, on average, every event in the synthetic catalog will produce more than

455   one aftershock in each generation of the simulation process. Therefore, the procedure does not converge and we consider the models $ETAS_\alpha$, $ETAS_\alpha^{b+}$, $ETAS_{bg, \alpha}$ and $ETAS_{bg, \alpha}^{b+}$ to be failing the retrospective consistency tests. This suggests that our approach of fixing the productivity parameter α during the inversion process is not suited to produce models that are consistent with reality in the long term. To avoid an underestimation of the productivity of large events without overestimating the overall productivity, differently parameterized productivity laws could be considered in the future. For instance, the logarithm of the

460   aftershock productivity might be better described as increasing quadratically rather than linearly with the magnitude of the triggering event. Furthermore, a branching ratio larger than one might be present during an ongoing sequence, but is not sustainable over a longer term. Thus, considering sequence-specific parameters or distinct productivity for mainshocks and

non-mainshocks, as done in the ETAS model employed by the USGS (van der Elst et al., 2022), would be promising aspects to explore in the future. In ETAS$_{\text{USGS}}$, a high branching ratio is also observed that could result in such exploding behavior during synthetic catalogs' simulation. However, due to the untapered temporal kernel that forecasts a relatively higher, when compared to the tapered ones, number of aftershocks in periods even after $\tau \approx 10^3$ days, many of the simulated aftershocks will be assigned a timing outside of our period of interest, effectively resulting in a much smaller branching ratio. This effect is so significant that these simulations do not only converge, but significantly underestimate the number of events.

In synthetic catalogs simulated based on the model ETAS$_0$, around 30% of the simulations have a higher event count than the observed value, and therefore the N-test is passed. However, the distance between the true observed magnitude distribution from the theoretical distribution estimated jointly from all the simulations is significantly higher than the distance between the observed magnitude distribution in each simulation and the theoretical distribution. The disagreement between the modeled and true magnitude distribution could be the result of either the true distribution not following a GR law with a single b-value, but rather a mixed distribution with b-values varying in time and/or space, or a bias caused by incompleteness potentially still present in the catalog. The quantile of the observed likelihood computed in spatial and pseudo-likelihood consistency tests is in the upper tail of the distribution of likelihoods of the synthetic catalogs. This indicates that the forecasts are describing the observed data 'suspiciously well', hence the result does not imply failure but requires further testing (Schorlemmer et al., 2007).

The magnitude distribution seems somewhat better in the ETAS variant that relies on the b-positive method for b-value estimation, ETAS$_0{}^{b+}$, which passes both the M-test and S-test - however, due to a significant underestimation of the event count, ETAS$_0{}^{b+}$ fails the N-test. On the other hand, ETAS$_{\text{bg}}{}^{b+}$, which uses the same seismicity rate map for placing the simulated background events and the same b-value estimate, fails the M-test. This is most likely due to a known issue of the test being dependent on the event count in simulated catalogs, which is somewhat, although not significantly, overestimated by ETAS$_{\text{bg}}{}^{b+}$, and is significantly overestimated by ETAS$_{\text{bg}}$. This flaw of the considered tests is further highlighted in the fact that ETAS$_{\text{USGS}}$, in contrast to ETAS$_0$, passes the M-test and S-test, despite the two models using identical spatial distribution of background events and aftershocks, and very similar b-values of 1 and 0.99. These findings suggest that the results of the M-, S-, and PL-tests should be interpreted with caution, and models should not be hastily rejected based solely on their performance in these specific tests.

Overall, we can conclude that ETAS models with fixed α clearly fail the long-term consistency tests. Among the remaining models, ETAS$_0$ and ETAS$_{\text{bg}}{}^{b+}$ pass the N-test, which is often considered the most crucial of consistency tests. Thus, we can consider these two variants as adequate choices for a first harmonized ETAS model for Europe. The other consistency tests provide additional information about the potential limitations of these models, which shall be addressed in future efforts to improve the models.

4.3 Results of pseudo-prospective tests

To compare the pseudo-prospective performance of one-day forecasts issued by the models, we visualize their cumulative information gain in Fig. 4(a). As introduced in Sect. 3.4, the log-likelihood score of a model is the logarithm of likelihoods

summed over space, and therefore always negative. The information gain is the difference between the log-likelihood scores of two models and is positive when the first model assigned a higher probability to the actual occurrence than the second model. The reference log-likelihood score to which we compare others in Fig. 4(a) is the one of the Poissonian time-independent base model. To determine whether one of the models is significantly outperforming another one, we apply the paired one-sided

500   t-test to the information gain values of the individual forecasting periods. In this way, we decide for each model pair whether the mean information gain (MIG) between the two models over all testing periods (shown in Fig. 4(b)) can be considered significantly positive or negative (significance shown in Fig. 4(c)).

The most prominent observation is the positive mean information gain of all ETAS models when compared to the time-

505   independent Poissonian model with ESHM20-informed background. All models except $ETAS_{bg,\,\alpha}$ and $ETAS_{USGS}$ achieve a significance level below 0.05. The three best performing models are $ETAS_0$, $ETAS_{bg}$ and $ETAS_0{}^{b+}$, which all significantly outperform all variants with fixed productivity term, and also show positive mean information gain to $ETAS_{bg}{}^{b+}$, without this result being significant according to the t-test.

To analyze the performance of the models more thoroughly, we observe the spatial component of their log-likelihood scores

510   by visualizing the total information gain over time for each spatial cell separately. The maps in Fig. 5(a–b) show the information gain between $ETAS_0$ and the time-independent model and between $ETAS_{bg}$ and $ETAS_0$, respectively. The spatial cells are joined into larger ones for better readability of the map. The more active areas show more pronounced total IG values, while no distinct spatial trends can be observed.

Discussion of the pseudo-prospective test results

515   That ETAS models outperform the time-independent model in one-day forecasting experiments is a result that could be expected, since the core strength of ETAS models is to model the short-term clustering behavior of earthquakes. The poor performance of the model variants with fixed productivity when compared to other ETAS variants could be explained by their tendency to overestimate the number of events, observed already during retrospective testing, when simulating over a longer period resulted in non-converging numbers of events. That the remaining model variants do not significantly outperform each

520   other suggests that they can all be considered adequate choices for short-term earthquake forecasting. This is further supported by the result that no spatial trend in model performance can be identified, and thus the models do not seem to be overfitting certain particular subregions.

5   Conclusions

In this paper, we calibrated and evaluated multiple variants of ETAS models to the highly heterogeneous dataset which sum-

525   marizes the recorded seismicity in Europe over the 35-year-long period between 1980 and 2015. The main result of seven years of pseudo-prospective one-day forecasting experiments is that ETAS-based models provide a significant information gain when compared to the time-independent benchmark model that underlies the ESHM 2020 hazard model. Additionally, the best-performing ETAS-based models inverted on the European dataset outperform the time-dependent ETAS model using

Figure 4. (a) Cumulative information gain through time, for consecutive non-overlapping 1-day windows over 7 years in the validation catalog. All models mentioned in Sect. 3 are compared to the Poissonian time-independent model, which acts as the null model. (b) Matrix of mean information gain of each model compared to all other models. Information gain in position (i, j) compares the score of the model in column j to the model in row i. (c) Matrix of p-values from paired one sided t-tests for each pair of models.
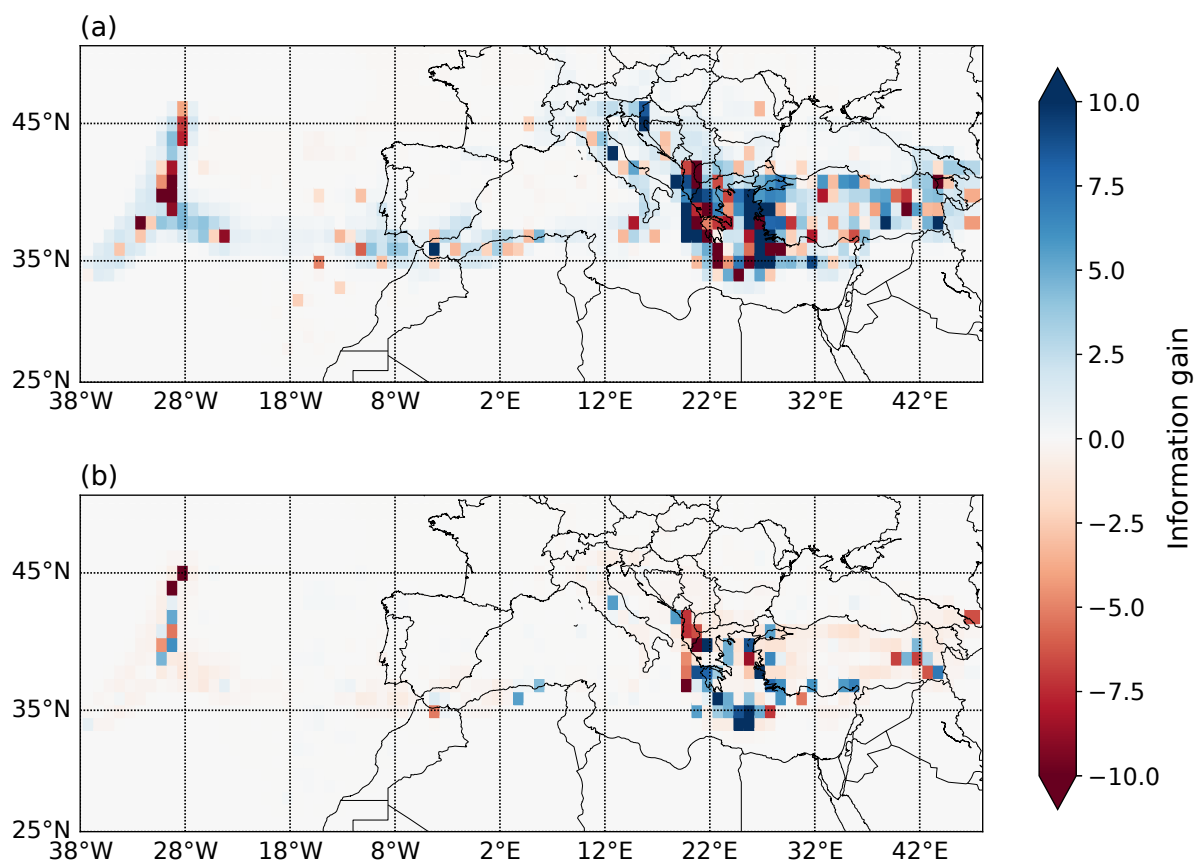
Figure 5. Total information gain per $1°$ lon $\times$ $1°$ lat spatial cell. Models compared: (a) $ETAS_0$ and time-independent Poissonian model. (b) $ETAS_{bg}$ and $ETAS_0$.

globally calibrated parameters. Besides a basic ETAS variant, we propose several modifications that, during model calibration,

530 allow the use of additional spatial information or fixing the productivity term of the model formulation. We found that fixing the productivity term to a higher value, which is suggested in the literature to overcome the underestimation of productivity of high-magnitude events, results in a highly overestimated branching behavior of events and an overall poor performance of a model that applies it. In future studies, other techniques to address the underestimation of the productivity of large events should be further explored. For ETAS variants that leverage information about the spatially varying background rate already during

535 the inversion, we found that the inferred parameters differ from those inferred using the basic approach, resulting in more events being interpreted as background events, and fewer as aftershocks. The background-informed ETAS variant achieves the highest mean information gain against the time-independent benchmark, though the performance difference to the second-best model is not significant. However, its background component contains additional information about long-term seismicity patterns, seismotectonic properties of the area, and seismicity in areas not represented in either the training or testing parts of the

540 catalog. For this reason, what could be the main strength of this method is hidden by the very limited size and time period of available testing data.

Retrospective long-term consistency tests provide an additional characterization of the strengths and weaknesses of each model variant, highlighting that two of the proposed model variants adequately capture the number of events over longer time periods. The magnitude consistency tests conducted for models using both the traditional maximum likelihood estimator of the

545 b-value as well as the b-positive estimator highlight potential areas of improvement of the proposed models. The simplification of using a single b-value to describe the magnitude distribution of all of Europe, as well as the assessment of the space-time variation of the catalog completeness provided through ESHM, may need to be revisited. Aside from the potential improvements of the issued forecasts by revisiting the completeness assessment, b-value variations, and strategies for sequence-specific model updating, our proposed models could be improved by adding further complexity, such as considering an anisotropic

550 spatial kernel of aftershock behavior.

In the process of real-time dissemination of earthquake forecasts, developing the model behind it is only the first step. The forecasts produced as the output of the introduced models are yet to be tested in a truly prospective manner. Recent CSEP efforts to establish a standardized open experiment format and the corresponding software support in performing such tests have resulted in the formation of the Floating Experiment, providing a suitable environment for future evaluation of the

555 properties of proposed models.

Another challenge in delivering earthquake forecasts operationally is the fashion of doing so: visualisation and communication of models' outputs are a topic of ongoing discussion among seismologists and communication experts (Field et al., 2016; Becker et al., 2018; Savadori et al., 2022). Both the layout and content of the final products depend on the use case in terms of the areas for which they are developed and the end users they serve, ranging from the wider public to civil protection services

560 to insurance companies. The main authority to communicate earthquake forecasts and act on them remains on local agencies and experts with knowledge specific to their area of interest. The role of the pan-European models presented here is to provide a harmonized "global" alternative less limited by administrative borders and information in areas where it would otherwise not be available.

Code and data availability. The training catalog with completeness assessments per tectozone and rate maps used as input here were pro-

565 duced by ESHM20 Danciu et al. (2021) and are accessible here. The continuation of the catalog used for testing is available here (Lammers et al., 2023). The ETAS inversion and simulation code used to train the models and generate the forecasts was developed for Mizrahi et al. (2021b), and is available at the Zenodo repository at https://doi.org/10.5281/zenodo.7584575 (Mizrahi et al., 2023c).

Author contributions. Conceptualization and Investigation: MH, LM, SW; Formal analysis, Methodology and Visualisation: MH, LM; Funding acquisition, Project Administration and Resources: SW; Software: LM, MH; Supervision: LM, SW; Writing - original draft preparation:

570 MH, LM; Writing - editing and review: all authors.

Competing interests. The authors declare that they have no conflict of interest.

Acknowledgements. This study has been funded by the European Union's Horizon 2020 research and innovation program under Grant Agreement Number 821115, real-time earthquake risk reduction for a resilient Europe (RISE), and by the EU project "A Digital Twin for Geophysical Extremes" (DT-GEO) (No: 101058129).

575   The authors wish to thank Shyam Nandan, Laurentiu Danciu and Aron Mirwald for their contributions, ideas and feedback.

References

Bayona, J. A., Savran, W. H., Iturrieta, P., Gerstenberger, M. C., Graham, K. M., Marzocchi, W., Schorlemmer, D., and Werner, M. J.: Are Regionally Calibrated Seismicity Models More Informative than Global Models? Insights from California, New Zealand, and Italy, The Seismic Record, 3, 86–95, https://doi.org/10.1785/0320230006, 2023.

580   Becker, J., Gerstenberger, M., Potter, S., Christophersen, A., and McBride, S.: Effective Communication of Operational Earthquake Forecasts (OEFs): Findings from a New Zealand Workshop, 2018.

Christophersen, A., Rhoades, D., Gerstenberger, M., Bannister, S., Becker, J., Potter, S., and McBride, S.: Progress and challenges in operational earthquake forecasting in New Zealand, 2017.

Crowley, H., Dabbeek, J., Despotaki, V., Rodrigues, D., Martins, L., Silva, V., Romão, X., Pereira, N., Weatherill, G., and Danciu, L.:
585   European seismic risk model (ESRM20), EFEHR Technical Report, 2, 2021.

Danciu, L., Nandan, S., Reyes, C. G., Basili, R., Weatherill, G., Beauval, C., Rovida, A., Vilanova, S., Sesetyan, K., and Bard, P.-Y.: The 2020 update of the European Seismic Hazard Model-ESHM20: Model Overview, EFEHR Technical Report, 1, publisher: ETH Zurich, 2021.

Field, E. H., Jordan, T. H., Jones, L. M., Michael, A. J., Blanpied, M. L., and Participants, O. W.: The Potential Uses of Operational
590   Earthquake Forecasting, Seismological Research Letters, 87, 313–322, https://doi.org/10.1785/0220150174, publisher: GeoScienceWorld, 2016.

Field, E. H., Milner, K. R., Hardebeck, J. L., Page, M. T., van der Elst, N., Jordan, T. H., Michael, A. J., Shaw, B. E., and Werner, M. J.: A spatiotemporal clustering model for the third Uniform California Earthquake Rupture Forecast (UCERF3-ETAS): Toward an operational earthquake forecast, Bulletin of the Seismological Society of America, 107, 1049–1081, 2017.

595   Grünthal, G. and Wahlström, R.: The European-Mediterranean Earthquake Catalogue (EMEC) for the last millennium, Journal of Seismology, 16, 535–570, https://doi.org/10.1007/s10950-012-9302-y, 2012.

Grünthal, G., Wahlström, R., and Stromeyer, D.: The unified catalogue of earthquakes in central, northern, and northwestern Europe (CENEC) - Updated and expanded to the last millennium, Journal of Seismology, 13, 517–541, https://doi.org/10.1007/s10950-008-9144-9, 2009.

Gutenberg, B. and Richter, C. F.: Magnitude and Energy of Earthquakes, Science, 83, 183–185, https://doi.org/10.1126/science.83.2147.183,
600   1936.

Hainzl, S., Zakharova, O., and Marsan, D.: Impact of Aseismic Transients on the Estimation of Aftershock Productivity Parameters, Bulletin of the Seismological Society of America, 103, 1723–1732, https://doi.org/10.1785/0120120247, 2013.

Helmstetter, A.: Is Earthquake Triggering Driven by Small Earthquakes?, Physical Review Letters, 91, 058 501, https://doi.org/10.1103/PhysRevLett.91.058501, 2003.

605   Jordan, T. H., Chen, Y.-T., Gasparini, P., Madariaga, R., Main, I., Marzocchi, W., Papadopoulos, G., Yamaoka, K., and Zschau, J.: Operational Earthquake Forecasting: State of Knowledge and Guidelines for Implementation., Annals of Geophysics, 2011.

Jordan, T. H., Marzocchi, W., Michael, A. J., and Gerstenberger, M. C.: Operational Earthquake Forecasting Can Enhance Earthquake Preparedness, Seismological Research Letters, 85, 955–959, https://doi.org/10.1785/0220140143, 2014.

Kagan, Y. Y.: Short-Term Properties of Earthquake Catalogs and Models of Earthquake Source, Bulletin of the Seismological Society of
610   America, 94, 1207–1228, https://doi.org/10.1785/012003098, publisher: GeoScienceWorld, 2004.

Lammers, S., Weatherill, G., Grünthal, G., and Cotton, F.: EMEC-2021 - The European-Mediterranean Earthquake Catalogue – Version 2021, https://doi.org/https://doi.org/10.5880/GFZ.EMEC.2021.001, gFZ Data Services, 2023.

Marzocchi, W. and Lombardi, A. M.: Real-time forecasting following a damaging earthquake, Geophysical Research Letters, 36, 2009.

Marzocchi, W., Lombardi, A. M., and Casarotti, E.: The establishment of an operational earthquake forecasting system in Italy, Seismological Research Letters, 85, 961–969, 2014.

Mizrahi, L., Nandan, S., and Wiemer, S.: The Effect of Declustering on the Size Distribution of Mainshocks, Seismological Research Letters, 92, 2333–2342, https://doi.org/10.1785/0220200231, 2021a.

Mizrahi, L., Nandan, S., and Wiemer, S.: Embracing data incompleteness for better earthquake forecasting, Journal of Geophysical Research: Solid Earth, 126, e2021JB022 379, publisher: Wiley Online Library, 2021b.

Mizrahi, L., Dallo, I., van der Elst, N. J., Christophersen, A., Spassiani, I., Werner, M., Iturrieta, P., Bayona, J. A., Iervolino, I., Schneider, M., Page, M. T., Zhuang, J., Herrmann, M., Michael, A. J., Falcone, G., Marzocchi, W., Rhoades, D. A., Gerstenberger, M., Gulia, L., Schorlemmer, D., Becker, J., Han, M., Kuralte, L. D., Marti, M., and Wiemer, S.: Development, Testing, and Communicating Earthquake Forecasts: Current Practices and Expert Recommendations, 2023a.

Mizrahi, L., Nandan, S., and Wiemer, S.: Developing and Testing ETAS-Based Earthquake Forecasting Models for Switzerland, in preparation, 2023b.

Mizrahi, L., Schmid, N., and Han, M.: lmizrahi/etas: ETAS with fit visualization, https://doi.org/10.5281/zenodo.7584575, 2023c.

Nandan, S., Ouillon, G., Sornette, D., and Wiemer, S.: Forecasting the full distribution of earthquake numbers is fair, robust and better, http://arxiv.org/abs/1903.07079, 2019.

Nandan, S., Kamer, Y., Ouillon, G., Hiemer, S., and Sornette, D.: Global models for short-term earthquake forecasting and predictive skill assessment, The European Physical Journal Special Topics, 230, 425–449, https://doi.org/10.1140/epjst/e2020-000259-3, 2021.

Nandan, S., Ouillon, G., and Sornette, D.: Are Large Earthquakes Preferentially Triggered by Other Large Events?, Journal of Geophysical Research: Solid Earth, 127, e2022JB024 380, https://doi.org/10.1029/2022JB024380, 2022.

Ogata, Y.: Statistical Models for Earthquake Occurrences and Residual Analysis for Point Processes, Journal of the American Statistical Association, 83, 9–27, https://doi.org/10.1080/01621459.1988.10478560, 1988.

Omi, T., Ogata, Y., Hirata, Y., and Aihara, K.: Intermediate-term forecasting of aftershocks from an early aftershock sequence: Bayesian and ensemble forecasting approaches, Journal of Geophysical Research: Solid Earth, 120, 2561–2578, https://doi.org/10.1002/2014JB011456, 2015.

Omi, T., Ogata, Y., Shiomi, K., Enescu, B., Sawazaki, K., and Aihara, K.: Implementation of a Real-Time System for Automatic Aftershock Forecasting in Japan, Seismological Research Letters, 90, https://doi.org/10.1785/0220180213, 2018.

Omori, F.: On the after-shocks of earthquakes, PhD Thesis, The University of Tokyo, 1895.

Savadori, L., Ronzani, P., Sillari, G., Di Bucci, D., and Dolce, M.: Communicating Seismic Risk Information: The Effect of Risk Comparisons on Risk Perception Sensitivity, Frontiers in Communication, 7, https://www.frontiersin.org/articles/10.3389/fcomm.2022.743172, 2022.

Savran, W. H., Werner, M. J., Marzocchi, W., Rhoades, D. A., Jackson, D. D., Milner, K., Field, E., and Michael, A.: Pseudoprospective Evaluation of UCERF3-ETAS Forecasts during the 2019 Ridgecrest Sequence, Bulletin of the Seismological Society of America, 110, 1799–1817, https://doi.org/10.1785/0120200026, 2020.

Savran, W. H., Werner, M., Schorlemmer, D., and Maechling, P.: pyCSEP: A Python Toolkit For Earthquake Forecast Developers, Journal of Open Source Software, 7, 3658, https://doi.org/10.21105/joss.03658, 2022.

Schorlemmer, D., Gerstenberger, M. C., Wiemer, S., Jackson, D. D., and Rhoades, D. A.: Earthquake likelihood model testing, Seismological Research Letters, 78, 17–29, https://doi.org/10.1785/gssrl.78.1.17, 2007.

650 Seif, S., Mignan, A., Zechar, J. D., Werner, M. J., and Wiemer, S.: Estimating ETAS: The effects of truncation, missing data, and model
     assumptions, Journal of Geophysical Research: Solid Earth, 122, 449–469, https://doi.org/10.1002/2016JB012809, 2017.

Tinti, S. and Mulargia, F.: Confidence intervals of b values for grouped magnitudes, Bulletin of the Seismological Society of America, 77,
     2125–2134, https://doi.org/10.1785/BSSA0770062125, 1987.

Utsu, T.: Aftershocks and Earthquake Statistics (II) : Further Investigation of Aftershocks and Other Earthquake Sequences Based on a New
655 Classification of Earthquake Sequences, 1971.

van der Elst, N. J.: B-Positive: A Robust Estimator of Aftershock Magnitude Distribution in Transiently Incomplete Catalogs, Journal of
     Geophysical Research: Solid Earth, 126, e2020JB021 027, https://doi.org/10.1029/2020JB021027, 2021.

van der Elst, N. J., Hardebeck, J. L., Michael, A. J., McBride, S., and Vanacore, E.: Prospective and retrospective evaluation of the U.S. Geo-
     logical Survey public aftershock forecast for the 2019-2021 Southwest Puerto Rico Earthquake and aftershocks, Seismological Research
660 Letters, 93, 620 640, https://doi.org/10.1785/0220210222, 2022.

Veen, A. and Schoenberg, F. P.: Estimation of Space–Time Branching Process Models in Seismology Using an EM–Type Algorithm, Journal
     of the American Statistical Association, 103, 614–624, https://doi.org/10.1198/016214508000000148, 2008.

Wiemer, S., Danciu, L., Edwards, B., Marti, M., Fäh, D., Hiemer, S., Wössner, J., Cauzzi, C., Kästli, P., and Kremer, K.: Seismic hazard
     model 2015 for Switzerland, Swiss Seismological Service (SED) at ETH Zurich, Zurich, pp. 1–163, 2016.

665 Zechar, J. D., Gerstenberger, M. C., and Rhoades, D. A.: Likelihood-Based Tests for Evaluating Space-Rate-Magnitude Earthquake Forecasts,
     Bulletin of the Seismological Society of America, 100, 1184–1195, https://doi.org/10.1785/0120090192, 2010.

Zechar, J. D., Marzocchi, W., and Wiemer, S.: Operational earthquake forecasting in Europe: progress, despite challenges, Bulletin of Earth-
     quake Engineering, 14, 2459–2469, https://doi.org/10.1007/s10518-016-9930-7, 2016.